Geochemistry, Geophysics, Geosystems®

AGU ADVANCING EARTH AND SPACE SCIENCES

RESEARCH ARTICLE
10.1029/2022GC010374

Seismic Imaging of the Westward Transition From Yakutat to Pacific Subduction in Southern Alaska

Florian Millet[1,2], Stéphane Rondenay[2], Thomas Bodin[1], and Carl Tape[3]

[1]Laboratoire de Géologie de Lyon, UMR 5276, Université de Lyon, Villeurbanne, France, [2]Department of Earth Sciences, University of Bergen, Bergen, Norway, [3]Geophysical Institute, University of Alaska Fairbanks, Fairbanks, AK, USA

Key Points:

- We apply a multi-mode 3D Kirchhoff migration to a new composite seismic data set from six arrays deployed in Alaska from 2000 to 2018
- We observe a sharp lateral boundary in the slab structure with a 10 km Moho step just offshore Anchorage from the Pacific to the Yakutat slab
- Our observations suggest that the crust is still partially uneclogitized down to 150 km depth in both slabs

Correspondence to:
T. Bodin,
thomas.bodin@ens-lyon.fr

Citation:
Millet, F., Rondenay, S., Bodin, T., & Tape, C. (2023). Seismic imaging of the westward transition from Yakutat to Pacific subduction in southern Alaska. *Geochemistry, Geophysics, Geosystems*, *24*, e2022GC010374. https://doi.org/10.1029/2022GC010374

Received 1 FEB 2022
Accepted 28 MAY 2023

Abstract Alaska is located at the northernmost point of the interface between the Pacific plate and the North American continent. The subduction of the Pacific plate generates arc volcanoes along the Aleutian trench, which stops to the east at the Denali Volcanic Gap. This volcanic gap has been linked to the underthrusting of the Yakutat terrane, which might alter the thermal state of the mantle wedge and prevent melt formation. This implies that the limits of the volcanic activity should mirror the extent of the Yakutat subduction. However, the transition from the Pacific slab to the Yakutat terrane at depth is not fully understood. To investigate this issue, we processed a new composite seismic data set from six arrays deployed in the region from 2000 to 2018. We apply a multi-mode 3D Kirchhoff migration to obtain high-resolution 3D scattering images of the region. Our results highlight a sharp lateral boundary in the slab structure, with a 10 km Moho step, just offshore Anchorage, and a more gradual slab transition beneath the southern part of the Kenai peninsula. Our images from the Yakutat slab plunge down to 150 km depth are consistent with previous estimates of the Yakutat slab extent below the Alaska Range. Although the steeply dipping boundaries of the subducting Pacific lithospheres are not fully recovered, deep coherent signals from the Pacific slab are observed down to 150 km depth. These observations suggest that the crust is still partially uneclogitized at these depths in both slabs.

1. Introduction

1.1. Geological Setting

Southern Alaska, located at the interface between the Pacific plate and the North American continent, comprises several superimposed geological units that were accreted by subduction over the past 160–220 My. In the western part of the study region, the Pacific plate currently subducts under south-central Alaska at about 5.5 cm/yr (Bird, 2003). The subduction is associated with a long volcanic arc which extends from the Aleutian islands to central southern Alaska at 152°W, where the volcanic activity stops, forming the Denali volcanic gap. Further east, the Wrangell volcanic field is the next and only large volcanic area before the Cascadia region (Rondenay et al., 2010).

In the eastern part of the study region, an oceanic plateau called the Yakutat terrane (G. L. Christeson et al., 2010) converges toward (and subducts under) North America at a similar rate as that of the Pacific plate (Figure 1). At the surface, the collision of the Yakutat terrane with the North American continent is accommodated by the right-lateral Fairweather Fault (Plafker et al., 1978). The boundary between the subduction of the Pacific slab and the collision of the Yakutat terrane hosts one of the most shallowly dipping subductions in the world, at an estimated 3° dip under the Kenai peninsula (S. Li et al., 2016). At depth, the estimated position of the subducted Yakutat terrane coincides with the Denali volcanic gap, and early studies suggest that the limit of the underthrusted Yakutat terrane is linked to a magnetic signal, the Slope Magnetic Anomaly (SMA, Saltus et al., 1999). This anomaly has been inferred to be of lower crustal nature, supporting the idea that the Yakutat terrane is a former oceanic plateau (Brocher et al., 1994). Offshore seismic studies confirm the different nature of the slab crust on either side of the SMA, showing a 10–15 km thick high-velocity layer on the eastern side that continues under the Prince William terrane, north of the surface expression of the Yakutat terrane, and a regular ~7 km thick Pacific crust on the western side (Brocher et al., 1994).

In the inland region, the distribution of intraslab seismic activity in southern Alaska shows a clear dichotomy (Eberhart-Phillips et al., 2006). Intermediate and deep seismicity along the Benioff plane in the western part of the study area can be seen in Figure 2. It shows a roughly 50° dip for the Pacific plate under the western part of

10.1029/2022GC010374

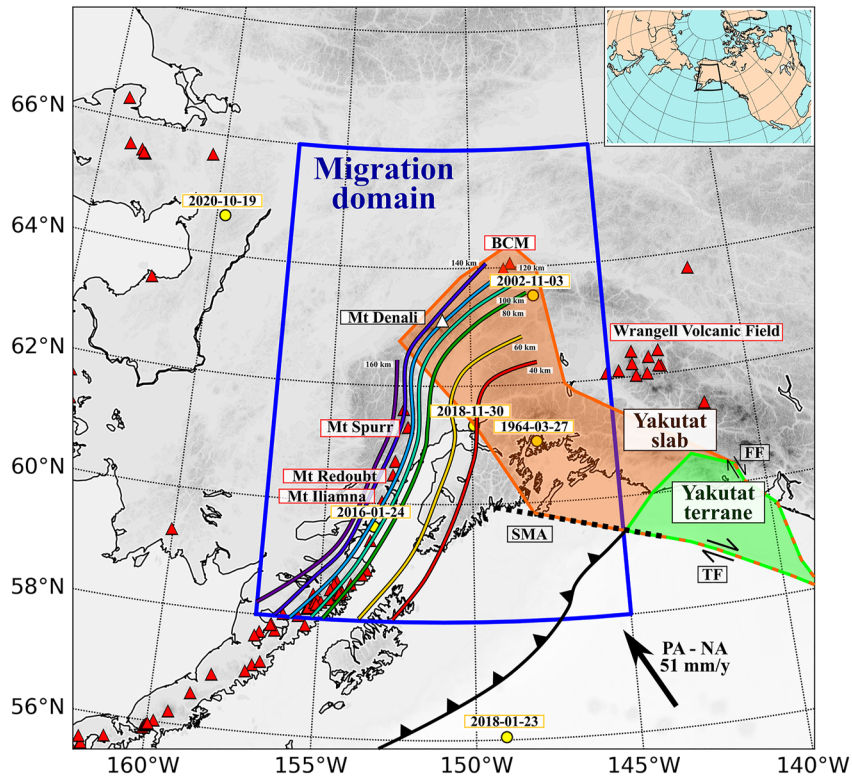

Figure 1. The map of southern Alaska with the migration domain highlighted in blue. The surface expression of the Yakutat terrane is shaded light green, while the extent of the subducted Yakutat slab in shaded orange (Eberhart-Phillips et al., 2006). Red triangles represent volcanoes, yellow circles represent large recorded seismic events. The depth of Wadati-Benioff seismicity is represented in colored contours with black outlines. BCM = Buzzard Creek Maars, SMA = Slope Magnetic Anomaly, PA = Pacific plate, NA = North American continent.

the study area under the SALMON array (code ZE). This dip angle gradually decreases to 10–30° to the east under the Multidisciplinary Observatory Of Subduction (MOOS) and BEAAR arrays (codes YV and XE, respectively) with no major gap or step in seismicity between the two regions (Chuang et al., 2017). On the eastern side, the deep seismicity is only visible north of 63°N. East of 150°W, the seismicity between 60°N and 62°N is almost flat, highlighting the low dip angle of subduction in this transition area, and intermediate depth seismicity completely disappears east of 148°W. These seismicity variations have been interpreted as one of the potential markers for the eastern limit of the Yakutat terrane (Eberhart-Phillips et al., 2006), with more recent studies of tremor activity pushing the limit even further East toward the Wrangell Slab (Wech, 2016).

The region is also prone to large earthquakes (Shennan et al., 2014). The largest recorded earthquake occurred on October 27, 1964, north and west of the Prince William sound and was of magnitude 9.2 (Ichinose et al., 2007). Recently, slow-slip events and low frequency earthquakes have been detected in the region. They have the potential to release as much energy as magnitude ~8 earthquakes over periods of 2–10 years (S. Li et al., 2016; Chuang et al., 2017). The region also produces large intraslab earthquakes, such as the 30 November 2018 Mw 7.1 event under Anchorage (Liu et al., 2019; West et al., 2020).

1.2. Seismic Imaging in the Region

The Yakutat terrane has been seismically imaged using local earthquake analysis (Daly et al., 2021), local earthquake tomography (Eberhart-Phillips et al., 2006; Nayak et al., 2020), teleseismic body wave (Ferris et al., 2003; Mann et al., 2022; Soto Castaneda et al., 2021) and surface wave analysis (Martin-Short et al., 2018; Wang & Tape, 2014) or a combination thereof (Berg et al., 2020; Gama et al., 2022), and active source experiments (e.g., G. L. Christeson et al., 2010; G. Christeson et al., 2013). Receiver function (RF) analysis using mainly data from the BEAAR temporary deployment in the northern part of the study area showed that the Yakutat crust

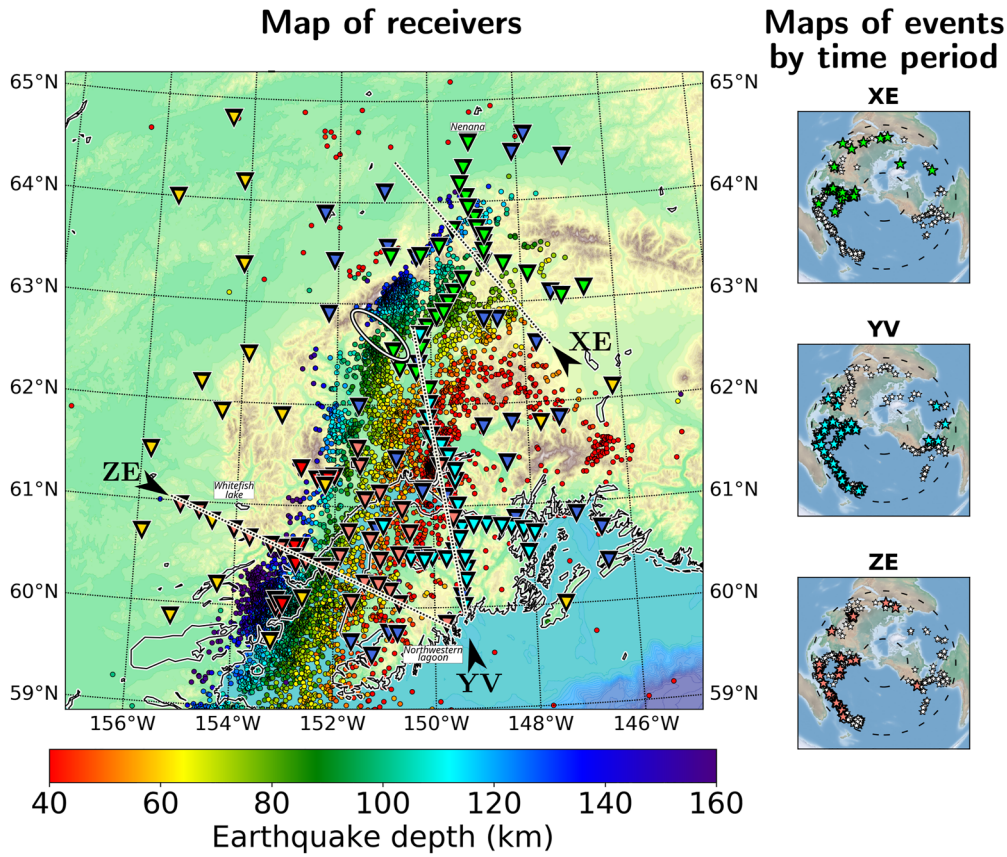

Figure 2. The distribution of receiver and events used in this study, along with Alaska Earthquake Center seismicity colored by event depth. The receivers are denoted by color-coded triangles. The arrays are as follows: green = XE, cyan = YV, salmon = ZE, blue = AK, red = AV and yellow = TA. The white stars on the event maps represent all events recorded during a given period, with the colored stars representing the selected events. The arrows and dotted lines on the left map represent the origin and orientation of the cross section in Figure 3, and the white circle highlights the seismicity gap observed by for example, Ratchkovski and Hansen (2002).

is 11–20 km thick with velocities up to 20% lower than the surrounding mantle (Chuang et al., 2017; Ferris et al., 2003; Mann et al., 2022; Rondenay et al., 2010). Local earthquakes and active seismic data show that the subducting Pacific plate in the western part of the study region has a thickness of 45–55 km, a 3%–6% higher Vp than the surrounding mantle, and 2–6 km thick, 5%–8% lower than the average low velocity layer at the top (Brocher et al., 1994; G. A. Abers, 2005). These data also show that the Yakutat terrane subducting in the east is 10–15 km thicker than the Pacific crust, in agreement with RF studies. In all body wave studies mentioned in this section, the Yakutat slab is imaged down to ∼140 km and is characterized by a low Vp and high Vp/Vs ratio, which is consistent with an oceanic plateau origin (Brocher et al., 1994; G. L. Christeson et al., 2010).

The mantle wedge above the subducted Yakutat crust is believed to be cold and may contain pieces of a Cretaceous aged slab (Eberhart-Phillips et al., 2006). This has implications for volcanism, as such mantle wedge conditions might impede melt production and/or upward migration of slab-released fluids, hence the reduced volcanic activity. These hypotheses are supported by thermal modeling of the state of the mantle wedge in the region (Rondenay et al., 2010). Based on their thermal models, Rondenay et al. (2010) postulate that the advance of a shallowly dipping slab causes a cooling of the mantle wedge above the source of slab fluids, which inhibits melt production and hence leads to diminished volcanic activity above the subducted Yakutat slab.

Moreover, recent studies have found that the mantle wedge below the Denali volcanic gap might be largely anhydrous (Plourde & Bostock, 2019; Yang & Gao, 2020). This lack of metamorphic fluids in the mantle wedge points to (a) a lower water content in the subducting slab or (b) increased water release depth. In combination with the cold nature of the subduction, the lower water content would increase the pressures at which the blue

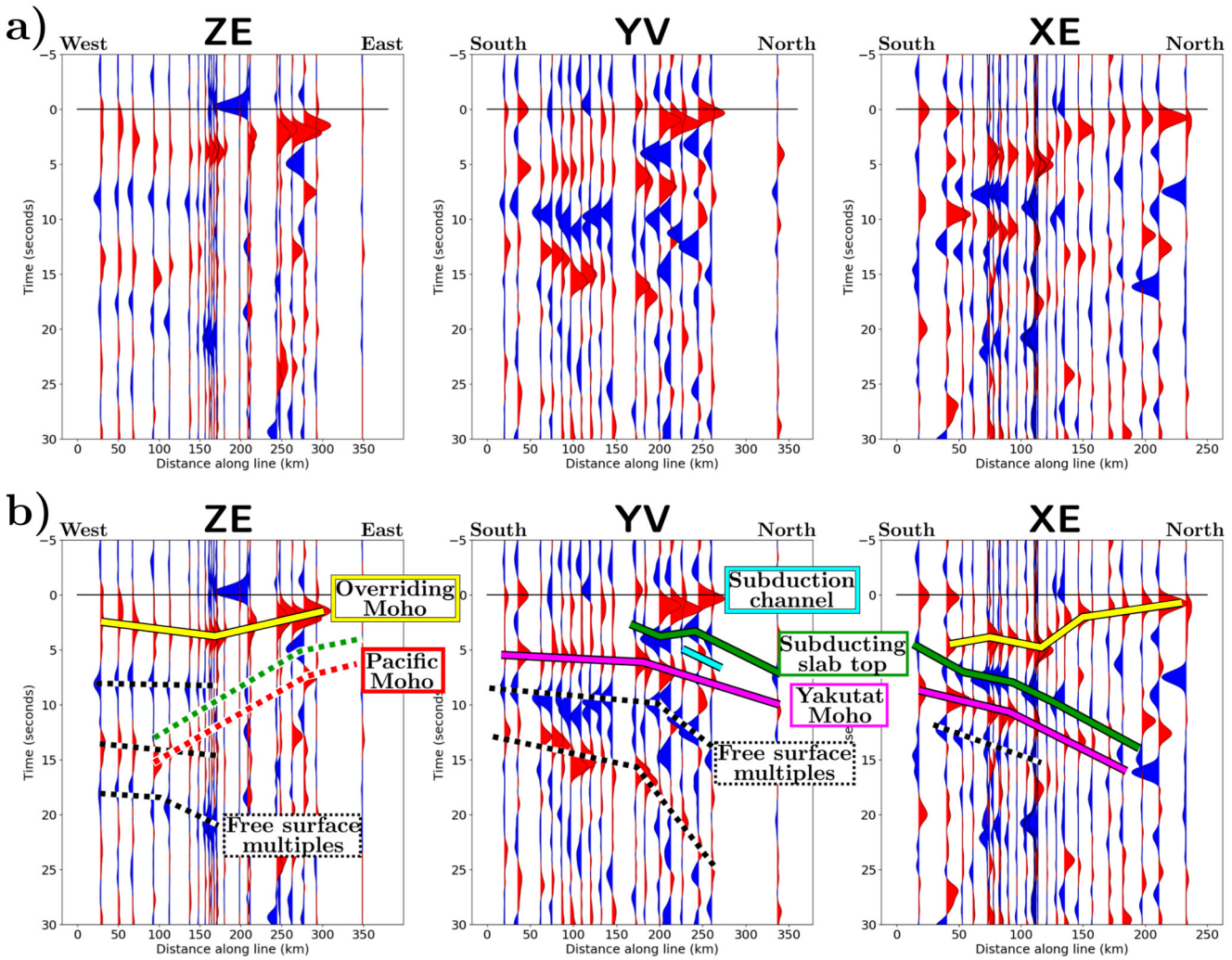

Figure 3. Normal move-out corrected and stacked radial receiver functions along the main axis of each of the three temporary arrays (a) without and (b) with preliminary interpretations of reflectors. Distance is taken from the west for SALMON, and from the south for Multidisciplinary Observatory Of Subduction and BEAAR (see Figure 2).

schist facies crustal rocks are stable. This delayed eclogitization is seen at depths of up to 130 km, and because uneclogitized crust presents a strong impedance contrast with the surrounding mantle, the subducting slab should be visible with RF imaging down to these depths (Plourde & Bostock, 2019).

Recently, the RF data set used in the first wave of high-resolution imaging studies (e.g., Ferris et al., 2003) has been extended all the way to the Kenai Peninsula (Kim et al., 2014). The expanded images are coherent with local 3D Vp models from for example, Eberhart-Phillips et al. (2006), and show a thickening of the slab and an increase in the dip angle across the boundary between the Pacific and the Yakutat slabs. However, the position and sharpness of the transition from the Pacific slab to the Yakutat at depth remains unclear. Only one previous 2D high-resolution RF image from Kim et al. (2014) crosses the previously published limit between the Yakutat and the Pacific slab in the south of the region, while the highest resolution 3D models have a grid spacing of 25 km in the same area - too low to resolve the boundary. In order to obtain a higher resolution image of the boundary along its entire extent, a 3D model of the scattering structure including all the additional data acquired since Kim et al. (2014) in the region is thus needed.

Here, we use a new composite data set to obtain 3D RF-based images of the region and compare the structure of the subducted slab across the previously published limit between the Pacific and Yakutat slabs. This data set is created by combining broadband seismic recordings from three temporary arrays deployed from 1999 to 2018,

with about 2 years of data for each array. We also use recordings from semi-permanent and permanent stations. The temporary arrays are mostly arranged in straight lines and perpendicular crosses. They are described in greater detail in Section 2. The data are processed and deconvolved to obtain receiver functions, which are sensitive to seismic phases in the coda of the direct P wave that corresponds to scattering from horizontal and lateral heterogeneities such as the Moho or differentiated lithospheric units. To obtain high-resolution 3D scattering structure images, we use a multimode 3D Kirchhoff migration developed by Millet et al. (2019). This method takes advantage of the three components of the recorded wavefield, as well as the signals from free surface multiples, to enhance the coherence of the migrated scattering potential. It is described in greater detail in Section 3. The results are shown in Section 4 and discussed in Section 5. They highlight different geometries and subduction dynamics between the west (Pacific crust) and the east (Yakutat terrane) of the Denali volcanic gap, with the former continuously steepening landward and the latter seemingly separated into two distinct dipping structures.

2. Data and Processing

2.1. A Composite Array for 3D Imaging

Seismograms recording distant earthquakes were collected from three temporary deployments as well as from other networks across southern Alaska (Figure 2) for distances ranging from 30 to 90 degrees of epicentral distance. The temporary arrays represent the densest part of this composite array. In order to maximize the quantity of data and minimize computation time, we considered only seismic events that occurred during one of the temporary deployments, that is, we do not consider events that happened when none of the temporary deployments were recording data. Hence, the combined ∼6 years duration (1999–2001, 2006–2008, 2015–2018) of these three deployments determines the number of earthquakes that were used in this study. The six arrays are shown in Figure 2.

The three temporary deployments are as follows. The northernmost array is the Broadband Experiment Across the Alaska Range (BEAAR, network code XE, green squares in Figure 2, Douglas Christensen (1999)) comprising 36 stations and operating between 1999 and 2001 as part of an IRIS/PASSCAL experiment (Ferris et al., 2003). Station spacing on the main NS line is just above 10 km. The second array, to the south of BEAAR, is the Multidisciplinary Observatory Of Subduction (MOOS, network code YV, light blue squares in Figure 2, Geoffrey Abers (2006)), comprising up to 34 stations operational between May 2006 and June 2008 (J. Li et al., 2013). Overall inter-station spacing is ∼11 km. Finally, the most recent deployment is the Southern Alaska Lithosphere and Mantle Observation Network (SALMON, network code ZE, pink squares in Figure 2, Carl Tape (2015)), comprising 28 stations operational during the time period 2015 to 2018 (Tape et al., 2017). Station spacing is quite variable with larger groups of stations ∼16 km away from each other and gaps of up to 40 km between them. Some stations (e.g., HOPE, NSKI, BING) are co-located across at least two deployments.

This composite array provides almost continuous coverage from Whitefish Lake (ZE.WFLW at 61°N,–155°E) west of the Cook Inlet to Nenana (AK.NEA2 at 64.5°N, –149°E) in the northern part of the region through the Northwestern Lagoon on the Kenai Peninsula (YV.HEAD at 59.8°N, –150°E). It crosses the previously published western limit of the Yakutat in the southern part of MOOS. The two main orientations are along-dip the Yakutat subduction on one side (BEAAR and MOOS) and along-dip the Pacific plate subduction (SALMON and southern part of MOOS).

The semi-permanent and permanent networks are as follows. The stations from the Alaska Regional Network (network code AK, dark blue squares in Figure 2, Alaska Earthquake Center (1987)) are located mostly around BEAAR and MOOS from −153° to −147° longitude. The Alaska Volcano Observatory (network code AV, red squares in Figure 2, Alaska Volcano Observatory/USGS (1988)) stations are distributed in clusters in the southwestern part of the study area around three main volcanoes (Spurr, Redoubt, Iliamna). Finally, the USArray Transportable Array (network code TA, yellow squares in Figure 2, IRIS Transportable Array (2003)) adds stations further away from the densest parts of the composite array for optimal coverage of the entire zone. They are mostly located west of −152° longitude and at the edges of the region. The combined AK and TA stations comprise 59 recording sites covering a roughly $3 \cdot 10^5$ km^2 area, resulting in an average inter-station spacing of ∼50 km.

2.2. Selecting and Processing of the Data

In order to extract three-component RFs, the data are processed via a multichannel workflow, similar to Rondenay et al. (2017). The raw teleseismic records are automatically downloaded from IRIS and rotated in the P-SV-SH

reference frame for each event. Throughout the selection steps, we perform three different automated quality checks. We first pre-select events that have a high signal-to-noise ratios (SNR) on the radial (R, SNR >5) and vertical (Z, SNR >10) components. We then reject traces that have low amplitude decay on the P component, that is, traces that have similar or more energy in the coda of the P wave than on the main arrival. This ensures that the signals do not exhibit an overly extended source time function (STF) or interference between multiple sources, which cause problems in the deconvolution. Finally, we select only events recorded on at least half of the active stations at the considered time. This is not necessary but allows to speed up the migration by avoiding computations for events that only bring limited information (see Section 3).

Once these high-quality events have been pre-selected, the onsets of the primary P wave are adjusted to their theoretical zero lag, and finely realigned on the actual P wave onset using a cross-correlation scheme on the P component. Note that because the direct P wave is confined to the P component (given an accurate enough 3D velocity model), the SV and SH components already represent mostly P-to-S scattered energy. A principal component analysis is performed for each event on the P component to separate the incoming coherent signal (first component, hereafter called P′) on all records from the variable (higher order components, hereafter called P″) part of the signal. The P′ component is interpreted as the STF for the event, and P″ is interpreted as the first order P scattering. Mathematically, we have $P'' = P–P'$ and the resulting system P″-SV-SH represents the entire three-component first-order scattered wavefield (Rondenay, 2009).

The three-component RFs are obtained through time-domain iterative deconvolution of the first-order scattered wavefield from the averaged STF with a Gaussian parameter width of 10, and are then filtered in the frequency band 0.03–0.5 Hz (Ligorria & Ammon, 1999). These frequencies correspond to wavelengths of 14 km at velocities of 7 km/s for P and 8 km at 4 km/s for the S-waves. As will be discussed in Section 3, free surface multiples have a vertical resolution of half of those wavelengths. Therefore, in order to improve the coherence in the migration, the frequency content of the data for different scattering modes can be adapted at a later stage in the multimode migration algorithm, as higher frequencies show better defined structures but lower frequencies allow for better stacking.

Before migrating the data using the 3D Kirchhoff algorithm, and for visualization purposes, the deconvolved data are stacked at individual stations using a 1D normal-moveout curve based on an average velocity model for the region (Figure 3). This helps to enhance the signal to noise ratio for near horizontal interfaces, but the 3D information is collapsed onto 1D. The stacked RF for the selected events is presented along with preliminary interpretations of reflectors. The overriding Alaskan Moho as well as the shallow part of the Yakutat slab are well defined but the free surface multiples are predominant at delay times of more than 10–15 s (Kim et al., 2014; Mann et al., 2022). We also note that the Pacific Moho, which is clearly visible on individual traces, is difficult to interpret in this 1D stack, hence the need for a fully 3D migration.

A final selection of traces is based on visual inspection of Kirchhoff migrated images for individual events. This means that during this last selection phase, we perform the migration for all the events individually, and we obtain depth images for the individual scattering modes (i.e., the direct and reflected waves, see Section 3). These different scattering modes can be individually selected or rejected on every event based on the coherence of the images across scattering modes, and the selected modes are combined in the final image. This is the only critical step during the selection process that is not automated.

2.3. Additional Data and Models

To perform the 3D migration, we use a 3D velocity model by Eberhart-Phillips et al. (2019), updated from Eberhart-Phillips et al. (2006). The Vp and Vp/Vs models were obtained using local earthquake arrival time tomography and active source data. As will be discussed in the next section, our migration method requires Vp and Vs models to compute the travel times for the various scattered phases. The 3D Vs model was computed by dividing Vp by Vp/Vs at each grid point, and we used the AK135 1D model (Kennett et al., 1995) to compute the teleseismic arrivals from the source to the computational domain. We did not try 3D models outside the computational region because we are using differential arrival times; hence, having a 3D model would not have a first-order effect on the shape of the wavefields that we correlate to obtain the migration ellipses.

To support the interpretation of our images, seismicity from the Alaska Earthquake Center (AEC) and previous results for the slab contour are plotted on top of Kirchhoff images (slab2, Hayes et al., 2018). Local seismic event

location data were obtained using permanent and temporary deployments across the entire state of Alaska. Only events that have reported location uncertainties of under 2 km are selected. They clearly outline the geometry of the subduction front. Slab2 outlines have been obtained through the compilation of several independent datasets, such as earthquake catalogs, active seismic studies, and bathymetry information (see Hayes et al., 2018, and references therein).

3. Methods

3.1. 3D Kirchhoff Migration

To obtain our high-resolution images of the subducted Pacific and Yakutat slabs, we used the migration method developed by Millet et al. (2019), where the fully 3D Kirchhoff imaging principle was adapted to teleseismic passive seismology. The method borrows from developments in active source seismic imaging, where dense acquisitions across relatively small areas allow for a dense and comprehensive 3D ray coverage of the subsurface (Hagedoorn, 1954).

Kirchhoff migration propagates scattered phases recorded at the surface back to all potential scattering points at depth where reflections and conversions occur. Based on travel time calculations, the RF is back-projected along elliptical migration isochrons, which represent all the points at depth that could contribute to a given phase observed at a given time in the recording. Actual scattering points are enhanced through constructive stacking over all the source-receiver geometries. The final stacked image depicts the impedance contrasts at the scattering interfaces and heterogeneities, which depend on the mineralogic composition and thermal state of the mantle and crust.

The method combines the efficiency of a 3D eikonal solver based on the fast marching method to predict travel times (FM3D, de Kool et al., 2006) with the first-order scattering calculations of amplitudes and polarities based on Ray-Born scattering. The migration is performed in a spherical 3D model with a 3D background velocity model. The resulting migrated images can be visualized by slicing through the 3D migration model on any given 2D cross-section. In this implementation of the Kirchhoff imaging principle, unlike comparable 2D and 2.5D methods such as the Generalized Radon Transform migration (GRT, Bostock et al., 2001), the positions of the receivers do not need to be projected along a line. This means that the energy is always migrated at its origin point in depth and that the resulting image under a given station will not depend on the orientation of the imaging line, but also that the sampling of the underlying medium in the migration area will be non-homogeneous. During the migration, an $i\omega$ filter is applied to the data to account for 3D wave propagation; hence, the discontinuities are interpreted in the middle of the scattering intensity anomalies.

This method is computationally efficient compared to other teleseismic migration methods, with a computational cost equivalent to that of advanced 2D and 2.5D migration methods such as the GRT migration (e.g., Bostock et al., 2001), albeit at the expense of not being able to retrieve absolute velocity variations but only scattering potential. It computes arrival times for all scattered phases at each point in the model with a single run of the eikonal solver. It treats each grid point in the migration model as a potential scattering point. Taking the gradient of the time fields and comparing the resulting orientation vectors for the incoming and outgoing waves allows us to compute the scattering angle at every grid point. By using scattering patterns based on the Ray-Born approximation, which can be found in for example, Wu and Aki (1985) or Beylkin and Burridge (1990), we predict the amplitude and polarity of the expected scattering. These scattering patterns are important for dipping discontinuities where polarity reversals can be problematic (Cheng et al., 2016). These methodological steps allow us to treat data from all incoming back-azimuths and slownesses correctly in an automated manner. We refer the reader to Millet et al. (2019) for more details on the method.

3.2. Multi-Mode Stacking

To obtain the best image and extract as much information from the data as possible, our method not only considers forward scattering (hereafter called PS) but also includes back-scattered waves from free surface multiples. These phases reflect off the Earth's surface as either P or S waves (lowercase p and s hereafter) and are scattered back up as either P or S waves (uppercase P and S hereafter), leading to four possible combinations: PpP, PpS, PsP, and PsS. The PsP mode is rarely used because its amplitude is usually much lower than that of the other

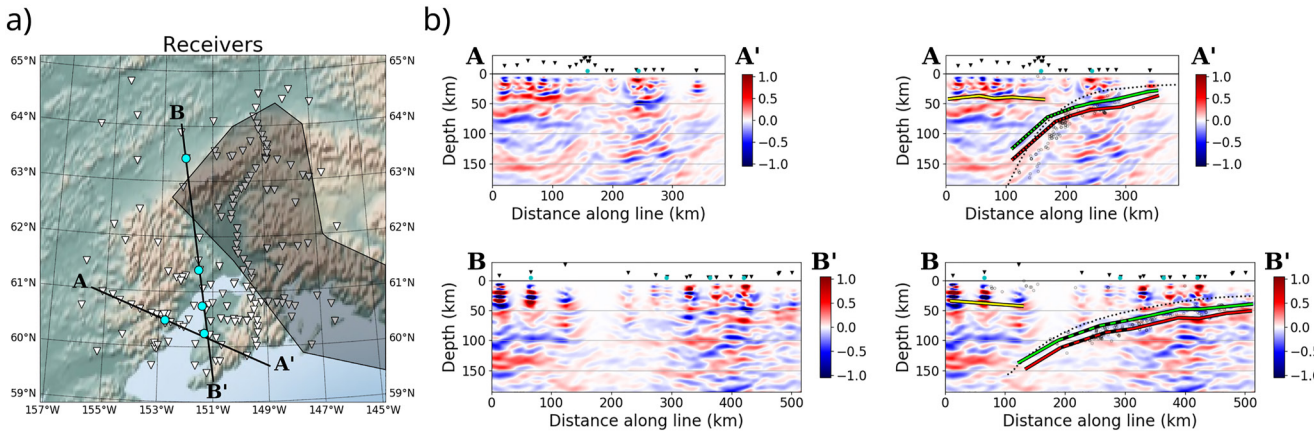

Figure 4. (a) Location of cross-sections through the regular Pacific slab. (b) Raw and interpreted cross sections. Interpreted boundaries include the slab top (green), the Pacific Moho (red), and the continental Moho (yellow). The black dotted line is the slab2 model, and circles represent the Alaska Earthquake Center seismicity.

phases and it has the same travel-time as the PpS mode for horizontal discontinuities. Note that the PsS mode can be further decomposed into PsSv and PsSh scattering as the S-to-S scattering can generate both Sv and Sh phases in the case of dipping discontinuities or anisotropy.

One of the properties of free surface reflections is that they have a higher vertical resolution power than the direct transmitted waves at the expense of a shallower maximum imaging depth (Rondenay et al., 2005). Our implementation of the Kirchhoff migration allows us to filter the waveforms independently on every mode to match their respective vertical resolutions and enhance the coherence of the stacked migrated image. Here we use the following higher corner frequencies for the different modes. The data are filtered to 1.0 Hz for the PS mode, 0.5 Hz for the PpP mode, 0.3 Hz for the PpS mode and 0.2 Hz for the PsSv and PsSh modes.

Different migrations are carried out separately for different modes of scattering. For example, in the PS migration, all observed phases migrate as if they originated from P-S conversions, and other scattered phases (PpP, PpS, and PsS) are spuriously migrated below their origin points, that is, they are undermigrated. Conversely, the PS scattered phases are spuriously migrated above their origin point in the free surface multiple migrations, that is, they are overmigrated. In this way, in each single-mode migration, only one type of scattering phase is correctly migrated. We resort to coherence filters to stack the different images obtained for different modes of scattering to enhance correctly migrated signals (see Millet et al., 2019, for details). In the migrated sections presented in Figures 4–6, we chose to give a higher coefficient to the PS migration than the multiples to preserve the deeper discontinuities, and hence we still observe some undermigrated features, especially under the overriding Moho signals on land.

4. Results

4.1. The Pacific Plate in the West

Here we describe the results from the 3D migration along 2D lines that follow or intersect the main structures of the subduction zone. Figure 4a shows the locations of the cross-sections under the western part of the study area, where we expect to image the normal Pacific slab. Given the position of the cross-section in the model volume, most of the migrated energy comes from stations from the ZE, AK, and AV networks.

Figure 4b shows the results for the Pacific plate. Line BB′ represents a roughly south to north cross-section at 151°–152°W. We observe a shallow negative signal, that is, a decrease in velocity with depth, that correlates with the shallowest part of the seismicity band from 40 km depth at 500 km offset to 65 km depth at 300 km offset. We associate this signal with the top of the subducted Pacific slab, with velocities decreasing from the overriding mantle to the subducting crust. This signal is followed by a positive signal approximately 8–10 km deeper, which is attributed to the subducting Moho. These signals have the same dip as the projection of the slab2 model onto the cross-section, albeit roughly 15 km deeper. The seismicity is mainly confined between these signal bands in the updip portion of the subduction system and crosses the subducted Moho into the slab's mantle at offsets lower than 300 km. The alternating signals can be seen again at ∼125 and 135 km depth, respectively, at 150 km offset close to the projection of the slab2 model. In the northern part of the cross-section (to the left), we

observe a positive signal between 40 km depth at 120 km offset and 30 km depth near point B, which is consistent with previous estimations of the overriding plate's Moho depth for this region (Feng & Ritzwoller, 2019; Zhang et al., 2019). The negative signal at ∼100 km depth and the positive signal at ∼140 km depth are associated with undermigrated free-surface multiples of the overriding Moho in the direct PS migration.

Line AA′ shows a NW-SE cross section under the densest linear part of the SALMON array. Starting under point A at the western end of the line, a shallow positive signal is observed steepening eastward from 35 km depth at origin to 45 km depth at 150 km offset. These depths are coherent with previous continental Moho picks (see e.g., Feng & Ritzwoller, 2019). Below this signal, we observe strong positive and negative signals at depths of ∼70 km. These correspond to undermigrated PpP and PpS energy in the dominating PS migration.

Beneath the Kenai peninsula (offsets of 220–340 km), line AA′ exhibits signals deepening westward associated with the Pacific slab. The negative slab top signal starts at 30 km depth close to point A′ and extends down to 50 km depth beneath the Cook Inlet. The positive slab Moho signal, that is, the increase in velocity with depth from crustal to mantle material, runs parallel about 10 km below the negative signal in this region, deepening from 40 to 60 km depth, and the seismicity stays within those two bands. Below the western part of the array, at offsets of 100–150 km, we observe a pair of deep coherent signals (∼120–150 km depth). The distance between the negative and positive signals is approximately 10 km. However, the feature outlined by these signals does not appear to be correlated with seismicity, as the two exhibit different dips (38° for the former vs. 50° for the latter). At 130 km depth, the feature seems to be offset from the seismicity horizontally by 40 km.

4.2. Yakutat Subduction in the North and East

Figure 5 shows the results under the densest parts of the MOOS and BEAAR deployments and in the northern part of the study area. Along line CC′, we observe three strong signals that follow each other from the origin to 200 km offset. The top negative signal associated with the Yakutat slab top starts at 25 km depth close to point C and dips down to 45 km depth at 250 km offset and 80 km depth at 360 km offset. The underlying positive signal is less than 10 km deeper and runs parallel to the slab top down to ∼180 km offset after which it disappears. These two consecutive signals have previously been reported by Kim et al. (2014) and have been linked to a subduction channel along the subduction interface. The bottom positive signal, which is thought to represent the Yakutat slab Moho, starts at 45 km depth and can be followed down to 60 km depth at 230 km offset before dipping more steeply to 100 km at 350 km offset. The two strong negative and positive signals, separated from each other vertically by ∼30–50 km and visible near 400 km offset, are interpreted as undermigrated PpS energy from the slab top and subducted Moho.

Along line DD′, the same succession of signals can be observed under the few stations at offsets lower than 300 km. Further to the north, where the station distribution is denser, we identify the top negative discontinuity from 60 km depth at 320 km offset to 130 km depth at 500 km offset. The bottom positive signal follows the same trend 20–25 km deeper, reaching 150 km depth at 480 km offset. Finally, a positive signal associated with the overriding continental Moho is observed on both cross sections. Along line CC′, the continental Moho stays flat from 430 km offset to point C′ at 35 km depth. Along line DD′, it starts at 45 km at the beginning of the Alaska Range at 380 km offset and gradually becomes shallower toward the end of the cross-section, where it reaches 30 km depth.

Lines EE′ and FF′ are NW-SE cross-sections that intersect the previous lines in the northern part of the region. They show the slab top dipping westward. Along line EE′, the negative Yakutat slab top can be seen from 60 km depth at 440 km offset down to 120 km depth at 220 km offset. Along line FF′, the slab top starts at 60 km depth at point F′ and deepens to 130 km depth at 230 km offset. In both cases, the Yakutat slab Moho positive signal follows the negative slab top, and the thickness of the crust is estimated at 20–25 km. The seismicity is completely contained within these two bands. These subducting signals are completely lost below 220 and 230 km offset, respectively, potentially highlighting the northern extent of the Yakutat terrane. Along line EE′, the continental Moho is seen at 35–45 km depth, with the deeper part being below the Alaska Range. Along line FF′, the continental Moho is seen at 35 km depth at 200 km offset. In both sections, we observe strong signals under isolated stations from the Western side of the lines (150–200 km offset). The consecutive negative/positive signals at ∼100 km/∼130 km depths have similar amplitude and vertical separation as the interpreted slab top and slab Moho. However, these stations are more than 100 km away from their nearest neighbor; hence, we do not see a

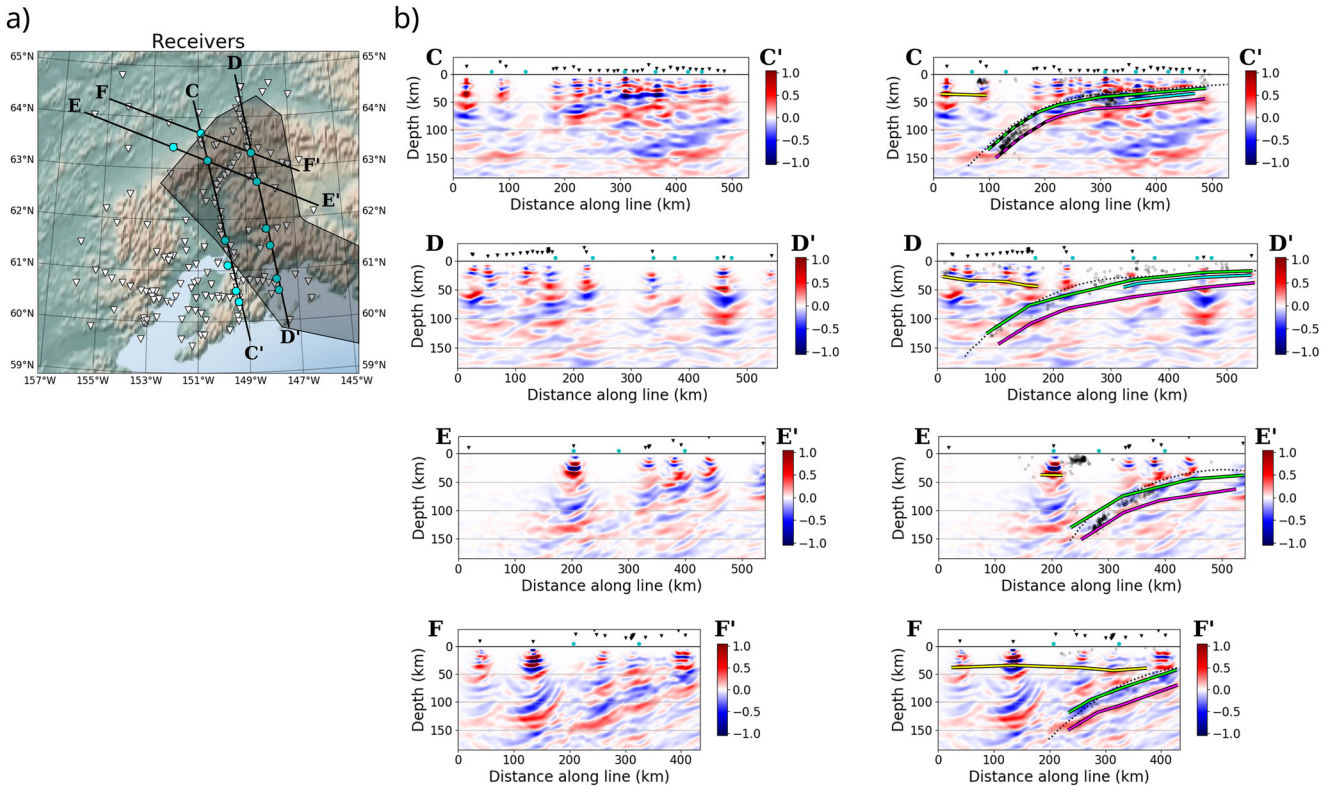

Figure 5. (a) Location of cross-sections through the thickened Yakutat subducting slab. (b) Raw and interpreted cross sections. Green is the slab top, magenta is the Yakutat Moho, cyan is the subduction channel inferred by Kim et al. (2014) and yellow is the continental Moho. See Figure 4 caption for other details.

continuity between these signals (which could be overmigrated subduction energy) and the slab interpretation further to the East.

4.3. Eastward Transition From the Pacific Plate to the Yakutat Slab

Figure 6 shows profiles that capture the boundary between the regular Pacific slab in the south west and the thickened Yakutat slab in the north east. Three lines (GG′, HH′, II′) are oriented SW-NE, and two (JJ′, KK′) are NW-SE. Line II crosses the previously published boundary of the Yakutat just north of Anchorage. In the Matanuska river region (offsets of 220–320 km), the results show a flat subduction interface, comprising a strong negative slab top signal at 35 km depth underlain by discontinuous positive subduction channel signals. The base of the Yakutat crust lies at 55–60 km depth. Further to the west, the slab top starts dipping westward and we identify the Pacific Moho as a positive signal 10 km below the slab top from 150 to 50 km offset. The subducting signals are lost at around 120 km depth. The boundary between the Pacific slab and the Yakutat, which appears at 160 km offset, displays a significant difference in crustal thickness. In both settings, the seismicity aligns with the imaged slab interfaces.

Just south of Anchorage, line HH′ shows the same boundary at around 200 km offset. The imaged Yakutat slab in this cross section has an estimated thickness of 25 km and a 9° dip angle toward the west. The deep signal associated with the Yakutat terrane stops below the two stations offshore Anchorage at 200 km offset. Below the Cook Inlet, the Pacific slab structure can only be inferred based on seismicity as the data in and around the basin are of lesser quality.

Line GG′ is located mostly under the EW branch of the MOOS array. The negative slab top signal gradually dips toward the west, starting at 25 km depth in the Prince William Sound (offsets larger than 300 km) and reaching 75 km depth below the Cook Inlet (offsets of 50–100 km). The shallow plate interface in the East at 40 km depth is consistent with results from for example, Mann et al. (2022) and model slab_{E115} from Jadamec and Billen (2010). The positive signal that directly follows below the slab top is interpreted as (a) the subduction channel in the eastern part of the cross section, and (b) the Pacific Moho in the western part. The positive signal

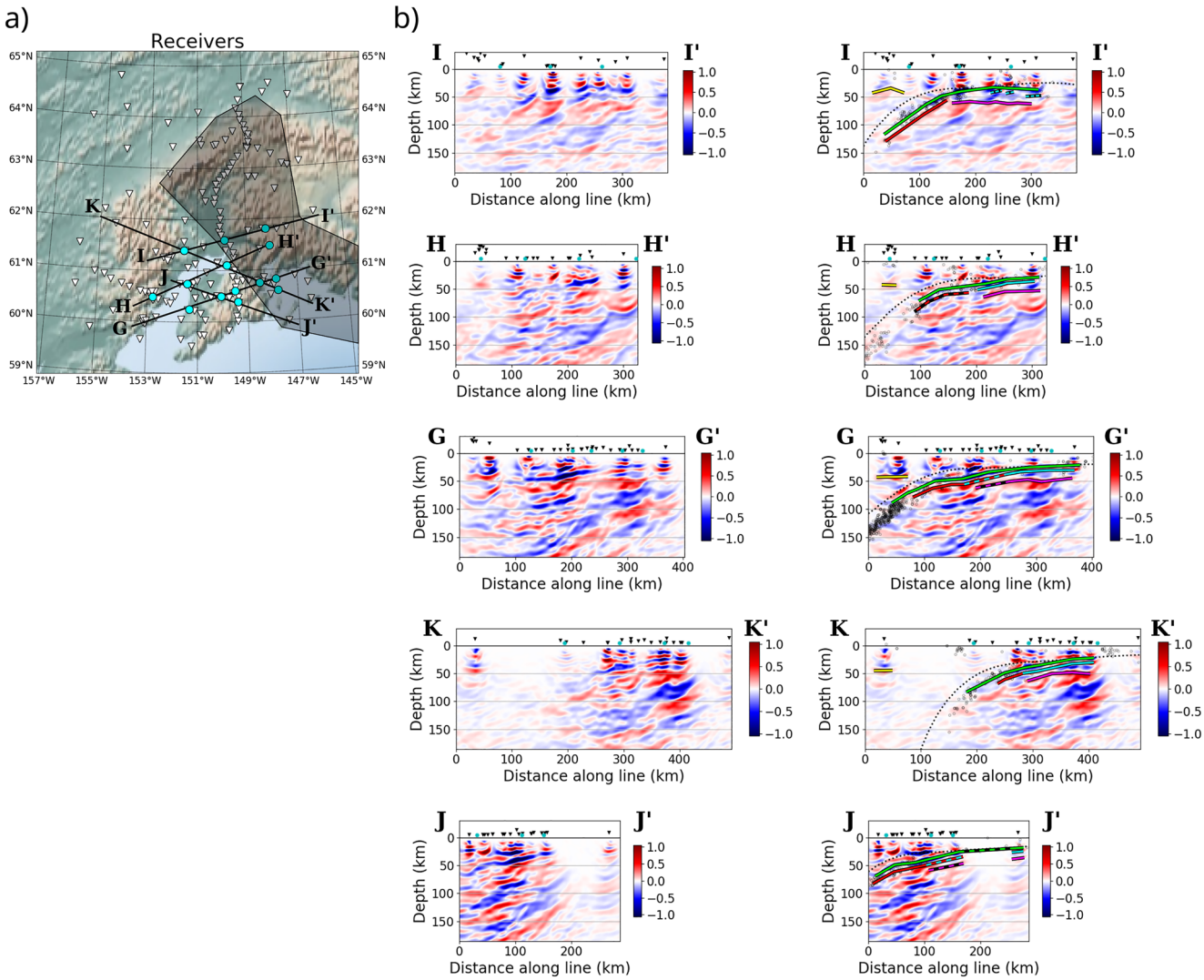

Figure 6. (a) Location of cross-sections through the transition from Pacific to Yakutat crust. (b) Raw and interpreted cross sections. Green is the slab top, magenta is the Yakutat Moho, cyan is the subduction channel inferred by Kim et al. (2014), yellow is the continental Moho and dark red is the Pacific Moho. See Figure 4 caption for other details.

associated with the Yakutat Moho is located at 50 km depth at 300 km offset. The boundary between the Yakutat and the regular Pacific slab occurs around 240 km offset, just east of where the two branches of the MOOS array cross each other. A gradual decrease in the amplitude and thickness of the signal associated with the Yakutat Moho can be seen from 260 to 210 km offset. The signal associated with the subduction channel in the west and the Pacific Moho in the east does not show a significant step; hence, the boundary between Yakutat and Pacific crust seems to be less sharp in the southern part of the region than in the central part (lines II′ and HH′). In this profile, the overriding Moho is imaged at around 40 km depth at ~50 km offset.

Line KK′ bridges the eastern part of the MOOS array with the stations across the Cook Inlet and toward the Alaska Range. The boundary between Pacific and Yakutat crust is observed below the two stations offshore Anchorage at 280 km offset, which confirms observations from line HH′. The subducting Pacific slab top can be followed from 50 to 80 km depth at a dip angle of 30°, with the Pacific Moho being 10–20 km deeper. Most of the seismicity is contained within the subducted crust. The subducting signals are lost below 200 km offset due to the lack of station coverage.

Along lines HH′, GG′, and KK′, we observe strong signals at ~70–120 km depth between 250 and 400 km offset. These signals exhibit dip angles that are 2–3 times steeper, and wavelengths that are 2 times larger, than

the overlying signals observed at ∼50 km depth. We interpret these deeper signals as mismigrated PpP and PpS energy within the dominating PS migration.

Finally, line JJ′ is located along the western part of the MOOS array. Only the easternmost station along this profile sits east of the previously published Yakutat-Pacific boundary. The triple signal associated with the Yakutat (negative, positive, positive) is observed at station P23K near point J′. In the western part of the image, seismicity follows the strong negative signal of the slab top and the subducting crust is 8–10 km thick, which corresponds to the regular Pacific subduction. Similar to line GG′, there is an ambiguous signal between 110 and 180 km offset which could represent a gradual Yakutat to Pacific transition.

5. Discussion

5.1. Imaging the Continental Alaskan Moho

The continental Alaskan Moho is imaged in all the cross sections located north of latitude 61°N. We observe a deeper Moho under the Alaska range, with depths up to 45 km under lines BB′ and DD′, than in the other areas, where it is observed at an average of 25 km (Northern end of line DD′) to 35 km depth (lines AA′ and FF′ e.g.,). These results are consistent with previous surface wave, ambient noise and RF studies (e.g., Berg et al., 2020; Feng & Ritzwoller, 2019; Gama et al., 2021).

South of the 61st parallel, we observe the over-riding Alaskan Moho clearly under lines AA′ and GG′, as well as under the cluster of stations near Mount Redoubt along line HH′. The relatively flat Moho at ∼35 km depth is coherent with previous studies (e.g., Zhang et al., 2019).

5.2. Imaging the Subduction Discontinuities

Our images allow us to refine the extent of the Yakutat terrane at depth, which is key to better assess the importance of the Yakutat in the formation of the Denali volcanic gap. In Figure 7, we draw all the points where we confirm or infer (yellow circles and red crosses respectively) the observations of the boundary between the regular Pacific and the thickened Yakutat crust. We also map the deepest imaged signals back to the surface for comparison with previous estimates of the northern extent of the Yakutat slab.

Except for the western end of cross-section AA′, all our images show clearly defined slab-top and Moho signals. Overall, our estimates of the subduction interface match the top of the seismicity envelope, and they are 2–10 km deeper than the slab2 estimates (Hayes et al., 2018). These results are consistent with observations by Nayak et al. (2020). For the shallow depths close to the subduction interface, the seismicity seems to extend into the overriding crust (e.g., Figure 5b line CC′, 6b line HH′). In places where we image the shallow Yakutat slab, the seismicity never extends below the subducting Moho (e.g., Figure 5b line CC′, 6b line GG′).

The deepest scattered signals from the Yakutat are imaged along lines DD′, EE′ and FF′ down to 150 km depth in the north of the study area, with previous results only reaching down to only 120 km depth (Kim et al., 2014). For the images that show the deepest parts of the slab, the seismicity is almost exclusively contained within the subducting slab, and the termination of the imaged slab signals corresponds to the extent of the deepest earthquakes (e.g., Figure 5b lines EE′ and FF′). If we assume that these signals track the maximal depth extent of the slab, then our observations of the limit of the Yakutat are coherent with previous estimations (e.g., Eberhart-Phillips et al., 2006, Figure 7).

Under the rectilinear SALMON array line, we observe coherent undermigrated signals that we associate with the Pacific slab top and Moho (Figure 8b). These signals are coherently observed on most single event migrations, regardless of the source-receiver geometry. They are present down to 150 km for the slab Moho and 130 km for the slab top. As described previously for the Yakutat slab, these signals line up with the maximal extent for the intra-slab seismicity. However, our imaging principle does not seem to be able to properly image the strongly dipping subducting slab (Figure 8b). Below 50–80 km depth, we start to observe a discrepancy between the migrated signals and the seismicity. At 150 km depth, the retrieved dip is ∼38°, while the slab2 model and seismicity outline yield slab dip estimates of 45–60°. The data coverage seems to be insufficient for our 3D Kirchhoff migration to recover such a high dip angle (Millet et al., 2019, Supporting Information). Nevertheless, we interpret this coherent signal as originating from the subducting Pacific slab.

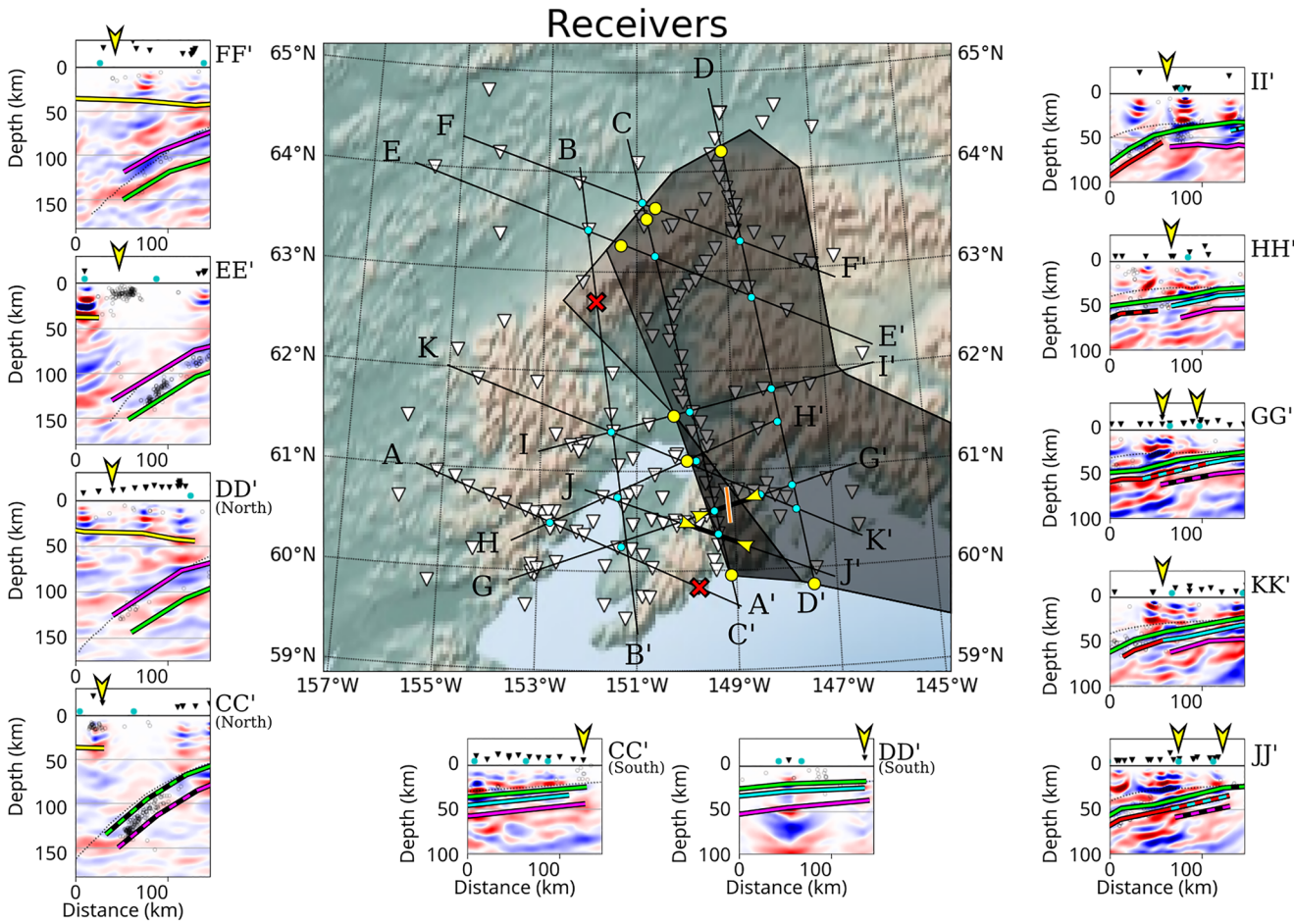

Figure 7. The location of the observed western and northern limits of the Yakutat slab. The sections are cut to 150 km length centered on the observed limits of the Yakutat slab, which are highlighted by yellow arrows on the migration line segments. Yellow circles on the map indicate the inferred sharp edge of the Yakutat at depth, and thick black lines with inward pointing arrows indicate smooth or ambiguous transition picks. Red crosses indicate no detection of the thick slab. Orange line represents a previous estimate of the transition below the Multidisciplinary Observatory Of Subduction array by Kim et al. (2014). Shaded area represents the extent of the slab at depth, with the lighter area removed from the previously published Yakutat extent and the darker area added to the estimate given by Eberhart-Phillips et al. (2006). See Figure 4 caption for other details.

5.3. Revisiting the Internal Structure and Lateral Extent of the Yakutat Slab

In the central part of the study region, the removed transition from the boundary between the Pacific and the Yakutat slab can be imaged precisely thanks to the high density of MOOS and AK stations. As seen in Figure 6, the boundary is laterally sharp in the vicinity and to the south of Anchorage (lines II′, HH′ and KK′). Here, a ∼10 km jump in crustal thickness occurs over a lateral distance of 30 km on average (Figure 8c). Moreover, the presence of the Yakutat slab is not observed below line BB′. This implies that the western limit of the Yakutat is closer to a NS axis than previously estimated (Figure 7).

In the southern part of the study area, the high density of MOOS stations has previously been used to highlight the western edge of the Yakutat slab beneath the Kenai peninsula Kim et al. (2014). Adding data from SALMON and AK stations, our observations below line CC′ show that the signal associated with the Yakutat Moho can be followed all the way to the southeast of the Kenai peninsula. Line CC′ intersects the western end of the Slope Magnetic Anomaly, which has been used to interpret the limit between Pacific and Yakutat south of Prince William Sound (Figure 1). The observations discussed here and in previous paragraphs are summarized in Figure 7, which proposes a revised outline of the Yakutat slab. The regions where previous interpretations of the western Yakutat are inconsistent with our new results are shown in light and dark gray shading, corresponding to contracted and expanded limits, respectively.

At depth, our images show a mostly uniform thickness for the Yakutat slab of ∼25 km from the trench to the deepest slab signals across most of its width. Where coverage is dense enough for the migration to perform at its

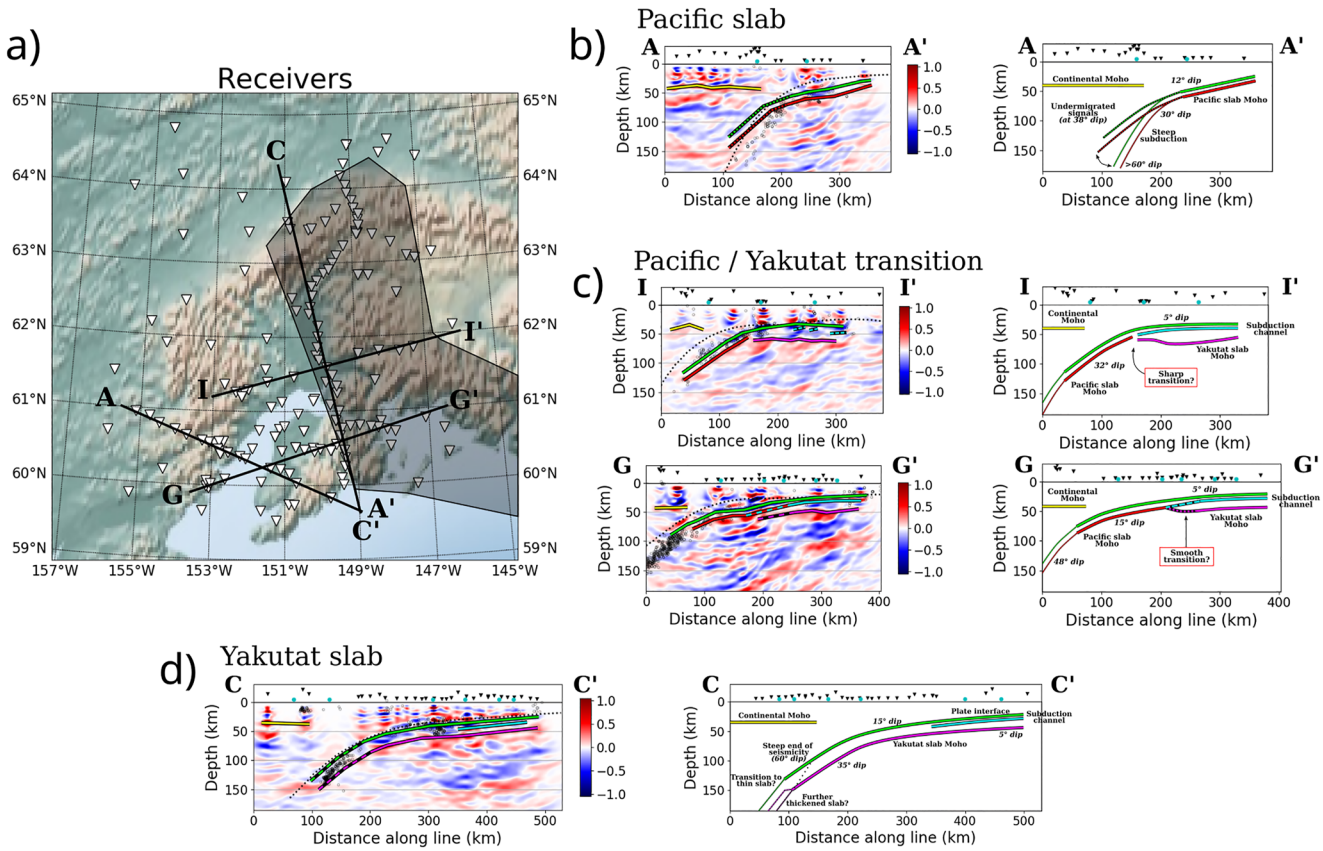

Figure 8. A summary of the results. (a) Map of the study area, along with interpreted observations and schematic representation of (b) the Pacific slab below SALMON data, (c) the two types of transitions from the Pacific to the Yakutat, and (d) the thick Yakutat slab in the western part of the study area. See Figure 4 caption for other details.

best, the Yakutat slab seems to be homogenous (e.g., Figure 5b line CC′, Figure 6b line KK′). However, in the EW lines GG′ and JJ′, the observed signals at the Pacific-Yakutat boundary exhibit lower amplitudes and suggest a thinner subducted crust beneath the Kenai peninsula compared to signals inside the commonly accepted limit of the Yakutat slab. Though these observations make our interpretation more ambiguous in the south, it appears that the transition here is more laterally gradational than in the north (Figure 8c).

What causes the Pacific-Yakutat boundary to change from being laterally gradational in the south of the study area (lines GG′ and JJ′) to being laterally sharp north of the Kenai peninsula (lines HH′, II′, KK′)? This variability in the sharpness of the boundary may be linked to variations in crustal thickness at the edge of the Yakutat slab. Further to the south-east (Figure 1), the boundary of the Yakutat terrane is marked by a large step (15–25 km) in crustal thickness along the Transition Fault. The size of this step has been shown to increase southeastward while the thickness of the sedimentary cover gradually decreases (G. Christeson et al., 2013; Worthington et al., 2012). Therefore, a Yakutat slab with thinner crust entering the trench at its western edge could explain the smooth transition observed beneath the Kenai peninsula. Deeper down in the subduction system, our images agree with previous observations of a ∼25 km thick Yakutat crust, which connects sharply to the regular Pacific crust (Yang & Gao, 2020).

The presence of a thick sediment layer above the Yakutat terrane, as observed offshore the subduction front, has been invoked to explain the existence of the low velocity layer interpreted as a subduction channel just beneath the slab top (Kim et al., 2014). We observe this subduction channel in the shallowly dipping Yakutat slab along line CC′ as well as across the entire width of the thickened slab along lines GG′ to KK′. This low velocity layer has the same polarity and roughly the same thickness as the imaged Pacific Moho to the east. These observations further highlight the difference between the southern and central parts of the study area (Figure 8c).

To the north of the study area, we rely on lines BB′, DD′, EE′, and FF′ to map the extent of the seismically visible Yakutat slab. There is no clear evidence for the presence of the Yakutat slab under the central portion of

line BB′, which contradicts previous estimates from for example, Eberhart-Phillips et al. (2006). Moreover, the gap between lines BB′ and CC′ corresponds to where authors such as Plourde and Bostock (2019) and Yang and Gao (2020) observe a gap in seismicity and high-velocity lithospheric structures respectively. These clues are interpreted as potential locations for the boundary from the Pacific to the Yakutat. Our images confirm that the Yakutat is indeed only visible to the east of this location, pushing the limit to the east in the northern part of the study area (Figure 7).

5.4. The Cold and Anhydrous Mantle Below the Denali Volcanic Gap

The internal thermal and mineralogical structures of the downgoing slabs influence the tectonic response of the rest of the subduction system (P. E. Van Keken et al., 2002), and the Yakutat subduction has long been thought to be one of the main causes for the Denali volcanic gap (Rondenay et al., 2008). Cold subduction zones, such as in Alaska, potentially allow for large quantities of water to be brought to intermediate depths (G. A. Abers et al., 2006). The water-bearing phases then break down and release that water at greater depths than in warmer subduction systems, causing deep seismicity and hydration of the mantle wedge. The absence of volcanism under the Denali region indicates that these processes are altered in southern Alaska.

The first clue pointing to an altered state is that the Yakutat slab subducts at a very shallow angle close to the trench. This is due to its high buoyancy, controlled by the thickened crust, which we map extensively along lines CC′ to II′. This shallow subduction cools the mantle wedge and prevents it from reaching partial melting conditions even in the presence of subduction fluids (Rondenay et al., 2010). The cold, but also relatively dry nature of the mantle wedge in the Alaskan subduction has been predicted by thermal modeling of this particular geometry, with an estimate of 10%–15% of the mantle wedge above 80 km depth being hydrated over the past 50 My using purely modeling approaches, and 10%–40% of hydration using Vp as a proxy for water content in a peridotitic mantle (G. Abers et al., 2017). However, Yang and Gao (2020) have found that this value does not represent the variability along the subduction zone. They observed lower velocities, that is, higher hydration values, in the shallowest parts of the mantle wedge south of 60°N, matching the along-strike extent of the thickest sedimentary layer entering the subduction zone. In the deeper part of the Yakutat mantle wedge, they observed significantly higher P-wave velocities, indicating a dry mantle wedge in the otherwise colder part of the subduction. Our observations show that the refined boundary between the regular Pacific slab and the thickened Yakutat slab also closely corresponds to the boundary between the steep region of the subduction and the shallowly dipping region of the subduction, that is, between the unperturbed "volcanic" profile in the West and the nonvolcanic profile above the Yakutat.

Another clue about the altered release of water from the subducting lithosphere can be found in the spatial correlation between deep scattering signals and seismicity. In our images, the deepest imaged slab signals disappear at the same depths as the deepest earthquakes. In recent upper mantle tomographic studies, the Pacific and Yakutat slabs can be observed as large high-velocity anomalies down to the mantle transition zone, with the Lithosphere-Asthenosphere Boundary (LAB) clearly visible only down to ∼120 km depth (see e.g., Jiang et al., 2018; Martin-Short et al., 2018). At the longer wavelengths of these models, there do not seem to be significant variations in properties along the plate interface in the first 200 km depth in the subducted slab. In this study, we observed the deepest P-to-S conversions from a subducted slab at 150 km depth, ∼30 km deeper than previously imaged in the area (Kim et al., 2014). The observations of the slab top in particular are coherent with the tomographic images discussed previously and the outlines from the slab2 model, matching them within a couple of degrees in dip and less than 10 km in depth at their deepest.

Moreover, the termination of the seismic activity within the slab seems to have a steeper dip than the slab itself (Figure 8d). This has been observed by several authors using 2D imaging methods that project the teleseismic data and local seismicity on an average projection line (e.g., P. Van Keken et al., 2012). Here, our fully 3D imaging principle allows us to image the migrated signals at their original location and to compare them directly with the deep seismicity. We observe this phenomenon mainly under lines CC′ and EE′ (Figure 5). This discrepancy in dip, also observed in other subduction zones at shallower depths, has been proposed to be due to the shape of the eclogitization front inside the subducted slab (P. Van Keken et al., 2012). By modeling the thermal conditions of the downgoing slab in typical subduction conditions, these authors find that the blueschist-to-eclogite transition has a steeper slope than the slab top itself. This mineralogic transition is the last of the major dehydration reactions in cold subducting slabs before they plunge down to the transition zone. These reactions are thought to

generate earthquakes through pore pressure increase and net volume decrease in cold slabs; hence, the associated seismicity would stop once the slab is completely eclogitized. In addition to this discrepancy in the dip angle, recent observations from Plourde and Bostock (2019) show that some of these deep earthquakes can be linked to either rapidly varying stress fields or fault weakening via eclogitization of the lower Yakutat crust. Taken together, the steep seismicity termination and this observation indicate that the slab could still contain meta-stable blueschist down to 150 km depth. Lower temperatures than average in the mantle wedge, caused by the shallow subduction angle toward the trench, increase the depths at which eclogitization is fully realized. This in turn delays the release of subduction fluids. These two effects both hinder melt generation, and could combine in the region above the Yakutat subduction to explain the absence of melt formation below the Denali volcanic gap.

6. Conclusion

This study provides a new 3D structural image of the southern Alaska subduction system based on seismic data from temporary and permanent recording networks that have operated in the region over the past 20 years. The results obtained data from the two older temporary networks are similar to the previously published images (BEAAR and MOOS, see e.g., Kim et al., 2014). The new images below the SALMON array, around the Cook Inlet, provide new constraints on a region that had not previously been imaged with such a high-resolution scattering-based method. Our estimates of overriding Moho depths are coherent with recent observations from, for example, Feng and Ritzwoller (2019) and Zhang et al. (2019). The limit between the Pacific and Yakutat slabs beneath southern Alaska is observed in multiple locations. We report these observations on a map to outline the subsurface extent of Yakutat subduction. Our observations are in general agreement with previous estimates of slab geometry (Eberhart-Phillips et al., 2006; Kim et al., 2014), but the boundary is interpreted as following a more NS-oriented trend than previously thought. The boundary is laterally sharp in the north, while the limit between the two slabs seems to be more diffuse around the Kenai Peninsula, where it meets the Slope Magnetic Anomaly. This might be due to a reduction in the thickness of the Yakutat slab along its Western edge from north to south.

With the caveat of not being able to retrieve dip angles greater than ~40° given the current coverage density, the 3D Kirchhoff images still provide valuable new information about the scattering structure in the region. While the 2D imaging methods, such as commonly used GRT migration, allow for fast and high density imaging, the 3D Kirchhoff scheme used here can resolve the subduction interfaces at oblique angles along the original station distribution (Millet et al., 2019). This allows us to capture the Pacific-Yakutat boundary. This boundary is marked by an abrupt change in crustal thickness of 5–10 km at depths of 60–80 km in the region around Anchorage, and a more gradual transition beneath the Kenai Peninsula. North of 64°N, the subducting signals disappear at the same depth as the seismicity, at approximately 150 km depth. To our knowledge, these are the deepest signals of subducted crust observed with scattered waves, and these results highlight the prominence of metastable blueschists and delayed eclogitization in the dynamics of the Alaskan subduction, and potentially other cold subduction zones. Together with the low-angle subduction in the shallow part of the southern Alaska subduction system, the seismically fast and cold nature of the mantle wedge and the presence of deep earthquakes linked to delayed eclogitization, our results explain the lack of melting in the system and the presence of the Denali volcanic gap above the Yakutat slab.

Conflict of Interest

The authors declare no conflicts of interest relevant to this study.

Data Availability Statement

The seismic data used in this study are archived at the Incorporated Research Institutions for Seismology (IRIS) and are accessible through the IRIS Data Management Center under the codes XE (Douglas Christensen, 1999), YV (Geoffrey Abers, 2006), ZE (Carl Tape, 2015), AK (Alaska Earthquake Center, 1987), AV (Alaska Volcano Observatory/USGS, 1988) and TA (IRIS Transportable Array, 2003).

Acknowledgments
The authors want to thank Editor Claudio Faccenna and reviewers Karen Fisher and Meghan Miller for their constructive suggestions that have significantly improved the manuscript. This study was partly funded by the Research Council of Norway under project Subduction Water and Metamorphism: a Modeling and Imaging Study (number 231354).

References

Abers, G., Van Keken, P., & Hacker, B. (2017). The cold and relatively dry nature of mantle forearcs in subduction zones. *Nature Geoscience*, *10*(5), 333–337. https://doi.org/10.1038/ngeo2922

Abers, G. A. (2005). Seismic low-velocity layer at the top of subducting slabs: Observations, predictions, and systematics. *Physics of the Earth and Planetary Interiors*, *149*(1–2), 7–29. https://doi.org/10.1016/j.pepi.2004.10.002

Abers, G. A., van Keken, P. E., Kneller, E. A., Ferris, A., & Stachnik, J. C. (2006). The thermal structure of subduction zones constrained by seismic imaging: Implications for slab dehydration and wedge flow. *Earth and Planetary Science Letters*, *241*(3–4), 387–397. https://doi.org/10.1016/j.epsl.2005.11.055

Alaska Volcano Observatory/USGS (1988). Alaska Volcano Observatory. *International federation of digital seismograph networks*. https://doi.org/10.7914/SN/AV

Alaska Earthquake Center, U. O. A. F. (1987). Alaska regional network. *International federation of digital seismograph networks*. https://doi.org/10.7914/SN/AK

Berg, E. M., Lin, F.-C., Allam, A., Schulte-Pelkum, V., Ward, K. M., & Shen, W. (2020). Shear velocity model of Alaska via joint inversion of Rayleigh wave ellipticity, phase velocities, and receiver functions across the Alaska transportable array. *Journal of Geophysical Research: Solid Earth*, *125*(2), e2019JB018582. https://doi.org/10.1029/2019jb018582

Beylkin, G., & Burridge, R. (1990). Linearized inverse scattering problems in acoustics and elasticity. *Wave Motion*, *12*(1), 15–52. https://doi.org/10.1016/0165-2125(90)90017-x

Bird, P. (2003). An updated digital model of plate boundaries. *Geochemistry, Geophysics, Geosystems*, *4*(3), 1027. https://doi.org/10.1029/2001gc000252

Bostock, M., Rondenay, S., & Shragge, J. (2001). Multiparameter two-dimensional inversion of scattered teleseismic body waves 1. Theory for oblique incidence. *Journal of Geophysical Research*, *106*(B12), 30771–30782. https://doi.org/10.1029/2001jb000330

Brocher, T. M., Fuis, G. S., Fischer, M. A., Plafker, G., Moses, M. J., Taber, J. J., & Christensen, N. I. (1994). Mapping the megathrust beneath the northern Gulf of Alaska using wide-angle seismic data. *Journal of Geophysical Research*, *99*(B6), 11663–11685. https://doi.org/10.1029/94jb00111

Carl Tape, D. H. C. (2015). Southern Alaska lithosphere and mantle observation network. In *International federation of digital seismograph networks*. https://doi.org/10.7914/SN/ZE_2015

Cheng, C., Bodin, T., & Allen, R. M. (2016). Three-dimensional pre-stack depth migration of receiver functions with the fast marching method: A Kirchhoff approach. *Geophysical Journal International*, *205*(2), 819–829. https://doi.org/10.1093/gji/ggw062

Christeson, G., Van Avendonk, H., Gulick, S., Reece, R., Pavlis, G., & Pavlis, T. (2013). Moho interface beneath Yakutat terrane, southern Alaska. *Journal of Geophysical Research: Solid Earth*, *118*(9), 5084–5097. https://doi.org/10.1002/jgrb.50361

Christeson, G. L., Gulick, S. P. S., van Avendonk, H. J. A., Worthington, L. L., Reece, R. S., & Pavlis, T. L. (2010). The Yakutat terrane: Dramatic change in crustal thickness across the Transition fault, Alaska. *Geology*, *38*(10), 895–898. https://doi.org/10.1130/g31170.1

Chuang, L., Bostock, M., Wech, A., & Plourde, A. (2017). Plateau subduction, intraslab seismicity, and the Denali (Alaska) volcanic gap. *Geology*, *45*(7), 647–650. https://doi.org/10.1130/g38867.1

Daly, K. A., Abers, G. A., Mann, M. E., Roecker, S., & Christensen, D. H. (2021). Subduction of an oceanic plateau across southcentral Alaska: High-resolution seismicity. *Journal of Geophysical Research: Solid Earth*, *126*(11), e2021JB022809. https://doi.org/10.1029/2021jb022809

de Kool, M., Rawlinson, N., & Sambridge, M. (2006). A practical grid-based method for tracking multiple refraction and reflection phases in three-dimensional heterogeneous media. *Geophysical Journal International*, *167*(1), 253–270. https://doi.org/10.1111/j.1365-246x.2006.03078.x

Douglas Christensen, R. H. (1999). Broadband experiment across the Alaska Range. In *International federation of digital seismograph networks*. https://doi.org/10.7914/SN/XE_1999

Eberhart-Phillips, D., Christensen, D. H., Brocher, T. M., Hansen, R., Ruppert, N. A., Haeussler, P. J., & Abers, G. A. (2006). Imaging the transition from Aleutian subduction to Yakutat collision in central Alaska, with local earthquakes and active source data. *Journal of Geophysical Research*, *111*(B11). https://doi.org/10.1029/2005jb004240

Eberhart-Phillips, D., Nayak, A., Ruppert, N., & Thurber, C. (2019). *Alaska 2018 update for USGSG18AP00017: Initial development of Alaska community seismic velocity models*. Zenodo. https://doi.org/10.5281/zenodo.2544925

Feng, L., & Ritzwoller, M. H. (2019). A 3-d shear velocity model of the crust and uppermost mantle beneath Alaska including apparent radial anisotropy. *Journal of Geophysical Research: Solid Earth*, *124*(10), 10468–10497. https://doi.org/10.1029/2019jb018122

Ferris, A., Abers, G. A., Christensen, D. H., & Veenstra, E. (2003). High resolution image of the subducted Pacific (?) plate beneath central Alaska, 50–150 km depth. *Earth and Planetary Science Letters*, *214*(3–4), 575–588. https://doi.org/10.1016/s0012-821x(03)00403-5

Gama, I., Fischer, K. M., Dalton, C. A., & Eilon, Z. (2022). Variations in lithospheric thickness across the Denali fault and in northern Alaska. *Geophysical Research Letters*, *49*(24), e2022GL101256. https://doi.org/10.1029/2022gl101256

Gama, I., Fischer, K. M., Eilon, Z., Krueger, H. E., Dalton, C. A., & Flesch, L. M. (2021). Shear-wave velocity structure beneath Alaska from a Bayesian joint inversion of Sp receiver functions and Rayleigh wave phase velocities. *Earth and Planetary Science Letters*, *560*, 116785. https://doi.org/10.1016/j.epsl.2021.116785

Geoffrey Abers, D. C. (2006). Multidisciplinary observations of subduction. In *International federation of digital seismograph networks*. https://doi.org/10.7914/SN/YV_2006

Hagedoorn, J. G. (1954). A process of seismic reflection interpretation. *Geophysical Prospecting*, *2*(2), 85–127. https://doi.org/10.1111/j.1365-2478.1954.tb01281.x

Hayes, G. P., Moore, G. L., Portner, D. E., Hearne, M., Flamme, H., Furtney, M., & Smoczyk, G. M. (2018). Slab2, a comprehensive subduction zone geometry model. *Science*, *362*(6410), 58–61. https://doi.org/10.1126/science.aat4723

Ichinose, G., Somerville, P., Thio, H. K., Graves, R., & O'Connell, D. (2007). Rupture process of the 1964 Prince William Sound, Alaska, earthquake from the combined inversion of seismic, tsunami, and geodetic data. *Journal of Geophysical Research*, *112*(B7), B07306. https://doi.org/10.1029/2006jb004728

IRIS Transportable Array. (2003). Usarray transportable array. In *International federation of digital seismograph networks*. https://doi.org/10.7914/SN/TA

Jadamec, M. A., & Billen, M. I. (2010). Reconciling surface plate motions with rapid three-dimensional mantle flow around a slab edge. *Nature*, *465*(7296), 338–341. https://doi.org/10.1038/nature09053

Jiang, C., Schmandt, B., Ward, K. M., Lin, F.-C., & Worthington, L. L. (2018). Upper mantle seismic structure of Alaska from Rayleigh and s wave tomography. *Geophysical Research Letters*, *45*(19), 10–350. https://doi.org/10.1029/2018gl079406

Kennett, B. L., Engdahl, E., & Buland, R. (1995). Constraints on seismic velocities in the Earth from traveltimes. *Geophysical Journal International*, *122*(1), 108–124. https://doi.org/10.1111/j.1365-246x.1995.tb03540.x

Kim, Y., Abers, G. A., Li, J., Christensen, D., Calkins, J., & Rondenay, S. (2014). Alaska megathrust 2: Imaging the megathrust zone and Yakutat/Pacific plate interface in the Alaska subduction zone. *Journal of Geophysical Research: Solid Earth*, *119*(3), 1924–1941. https://doi.org/10.1002/2013jb010581

Li, J., Abers, G. A., Kim, Y., & Christensen, D. (2013). Alaska megathrust 1: Seismicity 43 years after the great 1964 Alaska megathrust earthquake. *Journal of Geophysical Research: Solid Earth*, *118*(9), 4861–4871. https://doi.org/10.1002/jgrb.50358

Li, S., Freymueller, J., & McCaffrey, R. (2016). Slow slip events and time-dependent variations in locking beneath lower Cook Inlet of the Alaska-Aleutian subduction zone. *Journal of Geophysical Research: Solid Earth*, *121*(2), 1060–1079. https://doi.org/10.1002/2015jb012491

Ligorria, J. P., & Ammon, C. J. (1999). Iterative deconvolution and receiver-function estimation. *Bulletin of the Seismological Society of America*, *89*(5), 1395–1400. https://doi.org/10.1785/bssa0890051395

Liu, C., Lay, T., Xie, Z., & Xiong, X. (2019). Intraslab deformation in the 30 November 2018 anchorage, Alaska, Mw 7.1 earthquake. *Geophysical Research Letters*, *46*(5), 2449–2457. https://doi.org/10.1029/2019gl082041

Mann, M. E., Abers, G. A., Daly, K., & Christensen, D. H. (2022). Subduction of an oceanic plateau across southcentral Alaska: Scattered-wave imaging. *Journal of Geophysical Research: Solid Earth*, *127*(1), e2021JB022697. https://doi.org/10.1029/2021jb022697

Martin-Short, R., Allen, R., Bastow, I. D., Porritt, R. W., & Miller, M. S. (2018). Seismic imaging of the Alaska subduction zone: Implications for slab geometry and volcanism. *Geochemistry, Geophysics, Geosystems*, *19*(11), 4541–4560. https://doi.org/10.1029/2018gc007962

Millet, F., Bodin, T., & Rondenay, S. (2019). Multimode 3-D Kirchhoff migration of receiver functions at continental scale. *Journal of Geophysical Research: Solid Earth*, *124*(8), 8953–8980. https://doi.org/10.1029/2018jb017288

Nayak, A., Eberhart-Phillips, D., Ruppert, N. A., Fang, H., Moore, M. M., Tape, C., et al. (2020). 3D seismic velocity models for Alaska from joint tomographic inversion of body-wave and surface-wave data. *Seismological Society of America*, *91*(6), 3106–3119. https://doi.org/10.1785/0220200214

Plafker, G., Hudson, T. L., Bruns, T., & Rubin, M. (1978). Late Quaternary offsets along the Fairweather fault and crustal plate interactions in southern Alaska. *Canadian Journal of Earth Sciences*, *15*(5), 805–816. https://doi.org/10.1139/e78-085

Plourde, A. P., & Bostock, M. G. (2019). Relative moment tensors and deep Yakutat seismicity. *Geophysical Journal International*, *219*(2), 1447–1462. https://doi.org/10.1093/gji/ggz375

Ratchkovski, N. A., & Hansen, R. A. (2002). New evidence for segmentation of the Alaska subduction zone. *Bulletin of the Seismological Society of America*, *92*(5), 1754–1765. https://doi.org/10.1785/0120000269

Rondenay, S. (2009). Upper mantle imaging with array recordings of converted and scattered teleseismic waves. *Surveys in Geophysics*, *30*(4–5), 377–405. https://doi.org/10.1007/s10712-009-9071-5

Rondenay, S., Abers, G. A., & Van Keken, P. E. (2008). Seismic imaging of subduction zone metamorphism. *Geology*, *36*(4), 275–278. https://doi.org/10.1130/g24112a.1

Rondenay, S., Bostock, M. G., & Fischer, K. M. (2005). Multichannel inversion of scattered teleseismic body waves: Practical considerations and applicability. *Geophysical Monograph-American Geophysical Union*, *157*, 187.

Rondenay, S., Montési, L. G., & Abers, G. A. (2010). New geophysical insight into the origin of the Denali volcanic gap. *Geophysical Journal International*, *182*(2), 613–630. https://doi.org/10.1111/j.1365-246x.2010.04659.x

Rondenay, S., Spieker, K., Sawade, L., Halpaap, F., & Farestveit, M. (2017). Glimer: A new global database of teleseismic receiver functions for imaging Earth structure. *Seismological Research Letters*, *88*(1), 39–48. https://doi.org/10.1785/0220160111

Saltus, R. W., Hudson, T. L., & Connard, G. G. (1999). A new magnetic view of Alaska. *Geological Society of America Today*, *9*(3), 1–6.

Shennan, I., Barlow, N., Carver, G., Davies, F., Garrett, E., & Hocking, E. (2014). Great tsunamigenic earthquakes during the past 1000 yr on the Alaska megathrust. *Geology*, *42*(8), 687–690. https://doi.org/10.1130/G35797.1

Soto Castaneda, R. A., Abers, G. A., Eilon, Z. C., & Christensen, D. (2021). Teleseismic attenuation, temperature, and melt of the upper mantle in the Alaska subduction zone. *Journal of Geophysical Research: Solid Earth*, *126*(7), e2021JB021653. https://doi.org/10.1029/2021jb021653

Tape, C., Christensen, D., Moore-Driskell, M. M., Sweet, J., & Smith, K. (2017). Southern Alaska lithosphere and mantle observation network (salmon): A seismic experiment covering the active arc by road, boat, plane, and helicopter. *Seismological Research Letters*, *88*(4), 1185–1202. https://doi.org/10.1785/0220160229

Van Keken, P., Kita, S., & Nakajima, J. (2012). Thermal structure and intermediate-depth seismicity in the Tohoku-Hokkaido subduction zones. *Solid Earth*, *3*(2), 355–364. https://doi.org/10.5194/se-3-355-2012

Van Keken, P. E., Kiefer, B., & Peacock, S. M. (2002). High-resolution models of subduction zones: Implications for mineral dehydration reactions and the transport of water into the deep mantle. *Geochemistry, Geophysics, Geosystems*, *3*(10), 1056. https://doi.org/10.1029/2001gc000256

Wang, Y., & Tape, C. (2014). Seismic velocity structure and anisotropy of the Alaska subduction zone based on surface wave tomography. *Journal of Geophysical Research: Solid Earth*, *119*(12), 8845–8865. https://doi.org/10.1002/2014jb011438

Wech, A. G. (2016). Extending Alaska's plate boundary: Tectonic tremor generated by Yakutat subduction. *Geology*, *44*(7), 587–590. https://doi.org/10.1130/g37817.1

West, M. E., Bender, A., Gardine, M., Gardine, L., Gately, K., Haeussler, P., et al. (2020). The 30 November 2018 Mw 7.1 anchorage earthquake. *Seismological Research Letters*, *91*(1), 66–84. https://doi.org/10.1785/0220190176

Worthington, L. L., Van Avendonk, H. J., Gulick, S. P., Christeson, G. L., & Pavlis, T. L. (2012). Crustal structure of the Yakutat terrane and the evolution of subduction and collision in southern Alaska. *Journal of Geophysical Research*, *117*(B1), B01102. https://doi.org/10.1029/2011jb008493

Wu, R.-S., & Aki, K. (1985). Scattering characteristics of elastic waves by an elastic heterogeneity. *Geophysics*, *50*(4), 582–595. https://doi.org/10.1190/1.1441934

Yang, X., & Gao, H. (2020). Segmentation of the Aleutian-Alaska subduction zone revealed by full-wave ambient noise tomography: Implications for the along-strike variation of volcanism. *Journal of Geophysical Research: Solid Earth*, *125*(11), e2020JB019677. https://doi.org/10.1029/2020jb019677

Zhang, Y., Li, A., & Hu, H. (2019). Crustal structure in Alaska from receiver function analysis. *Geophysical Research Letters*, *46*(3), 1284–1292. https://doi.org/10.1029/2018gl081011